Nonparametric Image Registration of Airborne LiDAR, Hyperspectral and Photographic Imagery of Wooded Landscapes

Juheon Lee, Xiaohao Cai, Carola-Bibiane Schönlieb, and David A. Coomes

Abstract—There is much current interest in using multisensor airborne remote sensing to monitor the structure and biodiversity of woodlands. This paper addresses the application of nonparametric (NP) image-registration techniques to precisely align images obtained from multisensor imaging, which is critical for the successful identification of individual trees using object recognition approaches. NP image registration, in particular, the technique of optimizing an objective function, containing similarity and regularization terms, provides a flexible approach for image registration. Here, we develop a NP registration approach, in which a normalized gradient field is used to quantify similarity, and curvature is used for regularization (NGF-Curv method). Using a survey of woodlands in southern Spain as an example, we show that NGF-Curv can be successful at fusing data sets when there is little prior knowledge about how the data sets are interrelated (i.e., in the absence of ground control points). The validity of NGF-Curv in airborne remote sensing is demonstrated by a series of experiments. We show that NGF-Curv is capable of aligning images precisely, making it a valuable component of algorithms designed to identify objects, such as trees, within multisensor data sets.

Index Terms—Aerial photograph, hyperspectral image, image registration, light detection and ranging (LiDAR), remote sensing.

I. INTRODUCTION

AIRBORNE multisensor imaging is increasingly used to examine vegetation properties [1], [2]. The advantage of using multiple types of sensors is that each detects a different feature of the vegetation, so that collectively they provide a detailed understanding of the ecological processes [3]–[5]. Specifically, light detection and ranging (LiDAR) devices produce detailed point clouds of where laser pulses have been backscattered from surfaces, giving information on vegetation structure [6], [7]; hyperspectral sensors measure reflectances within narrow wavebands, providing spectrally detailed information about the optical properties of targets [3], [8]; whereas aerial photographs provide high spatial-resolution imagery so that they can provide more feature details, which cannot be identified from hyperspectral or LiDAR intensity images [9], [10]. Using a combination of these sensors, individual trees in tropical rain forests can be mapped, enabling invasive species to be monitored [8], [11], carbon storage to be assessed [12], and leaf physiological processes to be inferred [3], [13]. Accurate alignment of images is critical for the success of the aforementioned applications. However, images taken from different sensors or angles have relative rotation, translation or scale mismatches, and rugged terrain can cause complex displacement between images [14], [15]. As a result, aligning images is challenging.

Image registration involves transforming a template image T using a transformation φ so that it aligns with a reference image R. Alignment of remotely sensed images (known as image registration) is currently conducted with feature-based methods [1], [15]–[26], intensity-based methods [14], [27]–[34], or a combination of the two [15], [35], [36]. Feature-based methods rely on identifying common features in R and T. Using these common features, transformation parameters of feature-based methods are calculated such that the location of the features in the transformed template image T_{reg} are identical to those in R. Features in common between the reference and template images (i.e., points, patches or edges in the images), can be obtained by manual selection [15], [16], or by a variety of automatic techniques, including edge detection [1], [17], [18], scale-invariant feature transformation [19]–[22], [36], speeded-up robust features (SURF) detection [37], random sample consensus [23], [24], feature segmentation [21], [25], or phase congruency methods [26]. The performance of these approaches at detecting common features depends on image quality, and it can be difficult to locate corresponding features between images when data sets have different spatial resolutions or optical properties [27], [28]. Furthermore, in the case of multisensor imaging, some features in the reference image may not be present in the template image, or vice versa. In contrast, intensity-based methods involve maximizing the similarity in intensity values between the transformed template image T_{reg} and R [14], [27]–[30]. The most often used similarity measures are normalized cross correlation (NCC) [33], [34],

mutual information (MI) [28]–[30], [38], and normalized gradient fields (NGF) [31], [32]. In theory, intensity-based methods are fully automatic, but in practice, they are often mathematically ill-posed, in the sense that the registration solution might not be unique and a small change within the data might result in large variation in registration results [39]. In addition, different types of sensors affect the similarity between images significantly; therefore, the choice of similarity measure for the intensity-based methods is very important [2], [28]–[30], [35], [36], [38], [40], [41].

According to the form of the transformation φ used in image-registration methods, registration methods can also be classified as parametric or nonparametric (NP). Parametric registration methods use a set of parameters to construct φ; these parameters may, for example, be used to explicitly generate translation and rotation, or an affine transformation (i.e., one that preserves points, straight lines, and planes) [42]. In contrast, in a NP registration method the transformation φ is no longer parametrized, cf. Section III for details.

This paper develops a NP registration method, which we refer to as NGF-Curv, based on variational formulation as an alternative to the well-established feature-based and intensity-based approaches [15]. NP registration methods are already well-established in mathematical analysis, medical imaging communities, and computer vision [14], [43]–[50] but have yet to permeate far in the field of remote sensing. NP registration methods are based on a variational formulation within which a cost function is minimized. They have been developed to overcome the ill-posedness of established methods by considering not only the similarity between images but also the regularity of the transformation in the calculated cost function. These methods are not mentioned in recent reviews of registration methods in remote sensing [15], [51], and to the best of our knowledge, have never been used in this field. We demonstrate how NP registration can be used to register three types of airborne remote sensing data sampled over wooded landscapes (i.e., LiDAR, hyperspectral, and photographic imagery). The benefits of the NP registration method are illustrated, focusing particularly on its strong performance regardless of the number of different data types or degree of preprocessing. The data sets used to exemplify the approach are introduced in Section II. Then, in Section III, the mathematical concepts of the NP image registration algorithm based on variational formulation are introduced. The demonstration of the effectiveness of the approach is given in Sections IV and V. Finally, Section VI explores the behavior of alternative similarity measures and gives recommendations for future work.

II. DATA

This section briefly addresses the methodologies and properties of the data sets used for registration in this paper. Acquisition of remote sensing data sets was conducted in three areas of the Los Alcornocales Natural Park, Spain (lat $36°19'$, long $5°37'$) on 10 April 2011, by Airborne Research and Survey Facility of the U.K.'s Natural Environment Research Council (NERC-ARSF), and preprocessed by their Data Analysis Node. The study area is a typical Mediterranean wooded landscape,

where grassy fields in the valleys are surrounded by open woodland on hills, and rocky outcrops at higher altitude. The estimated tree cover area is 52% of the LiDAR survey area. The airplane flew at a nominal height above ground of approximate 3000 m and was equipped with LiDAR and hyperspectral imagers, as well as a digital camera. LiDAR [Leica ALS 50-II] emits pulses of monochromatic laser light (1064 nm) to scan topographical and geometrical structures of the surface, creating 3-D point clouds representing the points at which pulses are backscattered off surfaces and returned to the aircraft. A scan angle of $12°$ was used. Each point has an associated intensity value, which correlates with the proportion of a pulse's energy, which is returned to the sensor. However, the radiometric properties of LiDAR intensity are not completely known, LiDAR pulse intensity values are controlled by an automatic gain control (AGC) system during the acquisition process; thus, the intensity of the return is a function of unknown varying pulse energy, as well as the backscattering properties of the ground surface [52]–[54]. NERC-ARSF preprocessed these LiDAR data and georeferenced them to the Universal Transverse Mercator (UTM) projection with WGS-84 datum. The average LiDAR point density over the study site was 2 points per square meter (m²). In order to compare LiDAR imagery with other data sets in our experiment, LiDAR point clouds were projected onto a 2-D image plane by ignoring the height information for each LiDAR point. LiDAR intensity was calculated in 1-m pixels as the average of the all-return pulse intensities, with preprocessing by focal statistics function in ArcGIS software and image contrast enhancement by MATLAB build-in histogram equalization function `histeq`. Using first returns yielded qualitatively similar results to using all returns.

Hyperspectral imaging spectrometers measure solar energy reflected off the Earth's surface within a swath of land. Hyperspectral data were gathered using the AISA Eagle and AISA Hawk sensors (Specim Ltd., Finland), which are pushbroom sensors with 255 and 256 spectral bands covering 400- to 970-nm and 970- to 2500-nm wavelengths, respectively, across 2300-m swath width with 3-m spatial resolution. The hyperspectral sensors record reflected energy in digital numbers, which were converted to spectral radiance ($\mu Wcm^{-2} \cdot sr^{-1} \cdot nm^{-1}$) and then provided to us. Before image registration, hyperspectral imagery was atmospherically corrected using ATCOR-4 (Rese Ltd., Switzerland), which converts radiance values to reflectances. An accurate navigation system integrated with boresight calibrated hyperspectral sensors provides geocoordinates of each pixel in the hyperspectral imagery, which meant that the hyperspectral images could be orthorectified by digital elevation models (DEMs) from Advanced Spaceborne Thermal Emission and Reflection Radiometer and LiDAR data and then georeferenced to the UTM projection with WGS-84 datum. The estimated georeferencing error of hyperspectral image is about 5–10 m horizontally. However, it deteriorates at the edge of the field of view of the hyperspectral sensors. The spectral bands for a given scan line were all recorded simultaneously. True color composite of RGB bands (640, 549, and 460 nm) were converted to gray images by MATLAB build-in function `rgb2gray` and the gray image was used for registration purposes.

This article has been accepted for inclusion in a future issue of this journal. Content is final as presented, with the exception of pagination.

LEE *et al.*: NP IMAGE REGISTRATION OF LiDAR, HYPERSPECTRAL AND IMAGERY OF WOODED LANDSCAPES 3

Fig. 1. Aerial coverages of LiDAR (blue line), hyperspectral images (green line) and aerial photographs (red line) recorded in line 2 of the NERC-ARSF survey of Spanish woodland. The LiDAR aerial coverage is about 6.4 km^2 with 1-m spatial resolution, whereas the hyperspectral imagery and aerial photographs are 28.4 and 23.4 km^2, respectively. The spatial resolutions of hyperspectral imagery and aerial photographs are 3 and 0.3 m.

Aerial photographs were acquired during the flight using a Leica RCD-105 Digital Frame Camera. Each photograph has 7212×5408 pixels. Since the spatial resolution of aerial photographs is much higher than that of hyperspectral images, aerial photographs can help to identify objects more accurately. However, aerial photographs were not integrated with the aircraft navigation system; thus, they were not orthorectified or georeferenced during preprocessing. Metadata associated with aerial photographs informs of the time, location, and altitude of aircraft when each photograph was taken. We assumed that the location was the center of each image and that the spatial resolution of each pixel equaled to 0.3 m.

The aerial coverages and resolutions of LiDAR, hyperspectral images, and aerial photographs are given in Fig. 1. We can see that LiDAR imagery in blue line in Fig. 1 has a narrower width and smaller aerial coverage than the hyperspectral imagery (green) and aerial photographs (red). Our registration scheme aligns the hyperspectral imagery and aerial photographs onto the LiDAR image because combining three different types of sensors is the main purpose of this research.

If the preprocessed data had been georeferenced, then the images could have been aligned using the georeference coordinates. However, uncertainties from sensor distortions and boresight errors often cause misalignment; thus, image registration techniques need to be applied in order to precisely align images. Registration of aerial photographs onto hyperspectral images or LiDAR imagery is even more challenging because they were neither orthorectified nor georeferenced when delivered. This paper provides a robust and accurate approach for registering all three data sets.

III. METHOD

This section will briefly describe the mathematical concept of NP image registration, and the particular registration method NGF-Curv that we use for the registration of images in our data set (see [55] for further details). Let R and T be the given reference and template images, respectively, modeled as functions defined on a finite 2-D grid Ω and mapping a point x on the grid to a real intensity value $R(x)$ and $T(x)$, respectively. The resolutions of R and T do not necessarily have to be the same, which is they can have different sizes in vertical and horizontal directions. In this case, spline interpolation scheme was used to rescale them to the same grid Ω.

When registering template T with the reference image R, we find a suitable transformation, which maps T to R such that the transformed version of T is similar to R. This transformation maps the grid of T to the grid of R. A generic variational method for finding this transformation is as a solution $\varphi : \Omega \to \Omega$ of

$$\min_{\varphi} \left\{ \sum_{x \in \Omega} D\left[T\left(\varphi(x)\right), R(x)\right] + \alpha S(\varphi) \right\} \quad (1)$$

where D is a similarity measure that quantifies the difference between the distorted template T and reference image R, S is a so-called regularization term that imposes appropriate regularity on the transformation φ and α is a positive parameter that balances the importance of the similarity measure against the regularization term. Solutions of (1) for the registration problem are given by [43], [50], [56]. In the particular case of NP registration considered in this paper, the transformation function φ can be expressed as the sum of identity and displacement u, which is

$$\varphi : x \to x - u(x). \quad (2)$$

A standard choice for D in (1) is

$$D\left[T\left(\varphi(x)\right), R(x)\right] = \frac{1}{2}\left[T(x-u) - R(x)\right]^2$$

but this has the disadvantage of not being contrast-invariant [43]. This can be corrected by other kinds of distance measures, for example, NCC, MI, and NGF. The NCC distance measure is defined as

$$D^{\text{NCC}}[T_{\text{reg}}, R] = 1 - \frac{\left(\text{vec}(T_{\text{reg}})^T \text{vec}(R)\right)^2}{\left(\text{vec}(T_{\text{reg}})^T \text{vec}(T_{\text{reg}})\right)\left(\text{vec}(R)^T \text{vec}(R)\right)} \quad (3)$$

where T_{reg} denote the registered template after transformation to the reference image (i.e., $= T(\varphi)$), and $\text{vec}(A)$ generates a vector by concatenating the columns of the tensor A. This distance measures the normalized cross correlation between T_{reg} and R. The MI distance measure is defined as

$$D^{\text{MI}}[T_{\text{reg}}, R] = \sum_{x \in \Omega} \rho_{T_{\text{reg}}}(x) \log \rho_{T_{\text{reg}}}(x) + \sum_{y \in \Omega} \rho_R(y) \log \rho_R(y)$$
$$+ \sum_{x \in \Omega} \sum_{y \in \Omega} \rho_{[T_{\text{reg}}, R]}(x, y) \log \rho_{[T_{\text{reg}}, R]}(x, y) \quad (4)$$

where $\rho_{T_{\text{reg}}}$ and ρ_R are the marginal densities, and $\rho_{[T_{\text{reg}}, R]}$ is the joint density (see [43] for more details). In this paper, we use the NGF similarity measure [31], [43]. Here, the normalized gradient $\nabla I / |\nabla I|$ of an image I is used to measure similarity between R and T. More precisely, the NGF measure is defined as

$$\text{NGF}(I, \eta) = \text{vec}\left(\frac{\nabla I}{\sqrt{|\nabla I|^2 + \eta^2}}\right) \quad (5)$$

where $\eta > 0$ is an edge parameter. The edge parameter models the level of the noise present in I such that image values below

this parameter are ignored. Then the NGF distance measure is defined as

$$D^{\text{NGF}}[T_{\text{reg}}, R] = 1 - \left((\text{NGF}(T_{\text{reg}}, \eta))^T \, \text{NGF}(R, \eta) \right)^2 \quad (6)$$

which, if minimized, maximizes the linear dependency (alignment) of the NGF of T and R.

The regularization term S encodes the regularity that should be imposed on the transformation φ to reduce the ill-posedness of the registration problem. For an overview of different regularization terms and their effect on the registration (see [43] and [56]). In what follows, we use a curvature regularization [31], [50], which is

$$S^{\text{curv}}(\varphi) = S^{\text{curv}}(u) = \frac{1}{2} \sum_{x \in \Omega} |\Delta u(x)|^2. \quad (7)$$

This regularization results in the registration accuracy being dependent on the smoothness of the displacement u between R and T [56]. In particular, curvature regularization penalizes oscillations in u since it can be regarded as an approximation of the curvature of u [56]. One advantage of curvature regularization is that it does not require affine preregistration steps. Other regularization techniques, such as fluid registration [57], [58], are sensitive to affine linear displacement such that preregistration with affine linear transformation is required, see [50], [55], [56].

The method developed in this paper is based on minimizing the following function:

$$J(u) = \sum_{x \in \Omega} D^{\text{NGF}}[T_{\text{reg}}(x), R(x)] + \frac{\alpha}{2} \sum_{x \in \Omega} |\Delta u(x)|^2, \quad (\text{NGF-Curv})$$

where D^{NGF} is the NGF similarity measure defined in (6) and S^{curv} is the curvature regularization term defined in (7). In what follows, we refer to this method as the NGF-Curv method (NGF-Curv for short).

For the numerical minimization of (NGF-Curv) we use the *Image Registration software package* (FAIR).[1] There, the minimizer of (NGF-Curv) is computed iteratively via a semi-implicit scheme for the so-called Euler-Lagrange equation for (NGF-Curv). The latter is the equation that arises as the spatially discrete version of the Gâteaux derivative of the continuous functional J, which reads [50]

$$f(x, u(x)) + \alpha \Delta^2 u(x) = 0 \qquad \text{for } x \in \Omega \quad (8)$$

where $f(x, u(x))$ is the discretization of the derivative of the distance measure D. In order to solve (8) a semi-implicit

iterative scheme is used, which introduces an artificial time step Δt and computes the fixed point of

$$u^{k+1}(x) - \Delta t \alpha \Delta^2 u^{k+1}(x) = u^k(x) + \Delta t f(x, u^k(x)) \quad (9)$$

where $u^k(x)$ denotes the kth iterate of the scheme. Further details regarding discretization and numerical optimization are provided in [43]. Since remote sensing data sets contain large-scale surface information, it is computationally expensive to conduct entire image-registration steps at the original resolution [43]. FAIR provides a multilevel image registration scheme, producing a series of images varying in resolution, such that registration results from a coarser image can be used to initialize the registration on finer resolutions of the images. The multilevel scheme reduces the amount of expensive computation and the chance of being trapped in local minima during the iterative search, as images are much smoother in coarse resolution [43], [59].

IV. Application of the Registration Approach to the Airborne Remote Sensing Data Set

NGF-Curv requires that images are identical in size; thus, the first step of the process was to match the geographical boundaries of all data sets to each other, by reducing the number of features present in either R or T. Since both hyperspectral and LiDAR intensity images contain geocoordinates, geographical boundary matching of them is straightforward. However, the aerial photographs were neither georeferenced nor orthorectified and matching the boundary between aerial photographs and other data sets was therefore challenging. For the latter, we used the geocoordinate at which each photograph was taken as the center of each aerial photograph. Then, the geographic boundary of each aerial photograph was roughly calculated by counting the approximate number of pixels of an aerial photograph and adding 300 m in x and y directions to compensate the errors caused by rough approximation. Hence, the size of each aerial photograph image was assumed to be

$$L_{r_x} = 0.3 L_{t_x} + 300, \quad L_{r_y} = 0.3 L_{t_y} + 300$$

where L_{t_x} and L_{t_y} are the number of pixels of aerial photographs in x and y directions, and the 0.3 multiplier converts pixels into meters. Approximately, $L_{t_x} = 5000$ and $L_{t_y} = 7000$ for the photographs used in this paper.

Our objective is to coalign LiDAR, hyperspectral imagery, and aerial photograph. As the LiDAR aerial coverage was much smaller than other data sets (see Fig. 1), LiDAR was used as the reference image onto which the hyperspectral template image was aligned. LiDAR intensity data was used alongside a gray image converted from a true color composite (640, 549, and 460 nm) of the hyperspectral images using the MATLAB build-in function rgb2gray. Although it would seem natural to use the band at 1065 nm wavelength of the hyperspectral imagery, which corresponds to the LiDAR intensity wavelength, this band suffers from low signal-to-noise ratio, thus was not used.

NP image registration with a variational formulation finds the optimized location for each pixel that maximizes similarity between two images. This is achieved by numerical optimization

---

[1]MATLAB version of FAIR http://www.siam.org/books/fa06/.

This article has been accepted for inclusion in a future issue of this journal. Content is final as presented, with the exception of pagination.

LEE *et al.*: NP IMAGE REGISTRATION OF LiDAR, HYPERSPECTRAL AND IMAGERY OF WOODED LANDSCAPES   5

methods. The FAIR toolbox provides three different second-order optimization schemes: Gauss–Newton, l-BFGS, and Trust region. The l-BFGS optimization scheme was adopted in this paper. The choice of optimizer can influence the performance of image registration, but evaluating their performances was beyond the scope of this paper. NP registration yielded optimized spatial coordinates of each pixel, which were used for the transformation of original hyperspectral images. During the transformation, the hyperspectral images were resampled and regridded by nearest a neighbor method. Nearest neighbor estimates were chosen from existing values rather than averaging neighboring pixels, thus minimizing artifacts. This is important because hyperspectral imagery should preserve physically meaningful values.

Choosing optimal parameters in (NGF-Curv) is an important step of the registration process, but these are difficult to find automatically (although, see [31] and [60], for examples of automatic edge parameter η selection once noise level and image volume are known). We used a trial-and-error approach to find η and smoothness parameter α, which was time consuming. Fortunately, tuning of parameters for each registration of remote sensing images is not normally required, a single calibration for template and reference images taken by two different sensors was enough to obtain reasonable results in most cases. For the registration of a hyperspectral image onto a LiDAR intensity image the optimal values of α and η were found to be 5000 and 0.1, respectively.

The aerial photograph was aligned with the hyperspectral image because the swath widths of the hyperspectral images (2100 m) and aerial photographs (2400 m) were similar, whereas the LiDAR images were much narrower (800 m) (see Fig. 1). The narrow swath width of the LiDAR makes it difficult to find a region of interest in the aerial photograph corresponding to that in the LiDAR as the geographic boundary of the aerial photograph is roughly approximated, because of the roll, pitch, yaw of aircraft, and local topographic distortion. The registration of the aerial photographs onto the hyperspectral images is challenging because aerial photographs are distorted by various effects, including topography, lens distortion, and viewing angle. As we assumed the location where each aerial photograph was taken as the center of the image, corresponding hyperspectral images of size $L_{r_x} \times L_{r_y}$ m^2 were extracted from the hyperspectral imagery and used as the reference image. Curvature registration with NGF distance measure (NGF-Curv) was employed to register aerial photographs onto hyperspectral images. Regularization parameter was set to $\alpha = 2.5 \times 10^5$ and the edge parameter $\eta = 0.03$. RGB bands of hyperspectral images and RGB aerial photographs were both transformed to gray intensity images before registering them to each other to increase the processing speed and the robustness of the registration. After the registration of the aerial photographs onto the hyperspectral imagery, a mosaic of the aerial photographs was created, which was then aligned with the LiDAR data by applying the already computed LiDAR-hyperspectral imagery transformation.

Numerical experiments were conducted to compare the NGF-Curv method with well-known parametric registration methods based on alternative distance measures (i.e., NCC, MI,

TABLE I
MEAN, STANDARD DEVIATION, MINIMUM, AND MAXIMUM OF $|T_{\mathrm{REG}} - R|$, CORRELATION BETWEEN T_{REG} AND R, AND CPU TIME IN SECONDS OF EACH METHOD

		T	NCC	MI	NGF	SURF	NGF-Curv
Fig. 2	mean	73.70	66.89	73.08	72.63	74.56	65.68
	std	42.66	38.49	41.82	41.71	44.13	38.19
	min	0	0	0	0	0	0
	max	255	255	254	255	255	255
	corr	0.55	0.68	0.58	0.58	0.53	0.71
	time	-	4.48	6.63	6.96	5.86	34.85
Fig. 3	mean	52.94	48.66	48.73	48.92	48.67	47.09
	std	30.88	27.90	25.21	25.46	25.12	21.39
	min	0	0	0	0	0	0
	max	246	249	255	255	255	255
	corr	0.39	0.52	0.52	0.51	0.51	0.62
	time	-	10.33	11.23	15.76	163.28	380.12
Fig. 4	mean	55.61	51.37	47.09	49.01	48.61	45.23
	std	39.31	37.47	31.69	34.30	33.37	26.97
	min	0	0	0	0	0	0
	max	255	255	255	255	255	255
	corr	0.18	0.28	0.35	0.32	0.32	0.55
	time	-	9.70	11.91	14.21	197.38	375.02

and NGF) and the feature-based parametric method SURF [37]. These established methods are computationally efficient and widely used (see Sections I and III for references); SURF in particular is recognized as a robust local feature detector that is effective at feature-based parametric registration. Approaches were compared in terms of the mean, standard deviation (std), minimum (min), and maximum (max) of $|T_{\mathrm{reg}} - R|$, and the correlation (corr) between T_{reg} and R, using MATLAB build-in commands mean, std, min, max, and corrcoef, respectively. Mean and std reflect the distance between T_{reg} and R; thus, smaller magnitudes indicate better registration; min and max give the range of the differences between T_{reg} and R, whereas corr represents the linear dependence of T_{reg} and R (larger values indicate better registration). To compare computation efficiency, CPU time in seconds was given. All analyses were conducted using Intel Xeon E5-2630 2.30 GHz PC. Numerical experiments were conducted in LiDAR-hyperspectral registration and two different scenarios of aerial photograph-hyperspectral imagery registration. The reason why we give two examples of the aerial photograph-hyperspectral imagery registration is that topographical distortion of aerial photograph in rugged terrain may be larger than that in flat terrain.

V. EXPERIMENTAL RESULTS

Comparison of NGF-Curv with established approaches (Table I) show mean, standard deviation, maximum, minimum, correlation and computational time. The mean, standard deviation and correlation, in Table I support NGF-Curv performed better than NCC, MI, NGF, and SURF in all cases, whereas minimum and maximum errors show no difference. NGF-Curv requires more computational time than other methods in all examples. This is because NGF-Curv computes an optimal transformation of each pixel, whereas parametric methods find a set of transformation parameters. Therefore, the degree of freedom of NGF-Curv is much larger than that of NCC, MI, NGF, and SURF methods, thus slowing time. We now consider these results in detail.
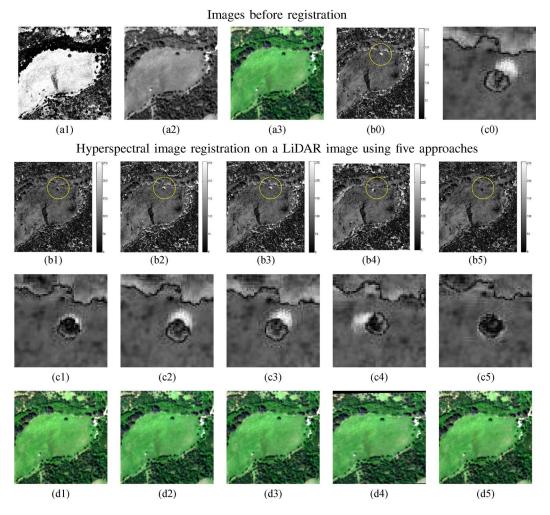
Images before registration

Hyperspectral image registration on a LiDAR image using five approaches

Fig. 2. Image registration of a hyperspectral image onto a LiDAR intensity image of a Spanish woodland, surveyed by aircraft (scale 400×400 m^2). The first row shows (a1) a LiDAR intensity reference image R; (a2) a hyperspectral template image T; (a3) original color image of (a2); (b0) a map showing the difference between T and R (i.e., $|T - R|$), which would be entirely dark if the match was perfect; (c0) highlights the circled area of (b0). The second row of maps show $|T_{\text{reg}} - R|$ obtained by using established methods NCC, MI, NGF, SURF, as well as our NGF-Curv method. The results of registration methods are denoted by $T_{\text{reg}}^{\text{NCC}}$, $T_{\text{reg}}^{\text{MI}}$, $T_{\text{reg}}^{\text{NGF}}$, $T_{\text{reg}}^{\text{SURF}}$, and $T_{\text{reg}}^{\text{NGF-Curv}}$, respectively, in these panels; yellow circle highlights areas of the images where differences among registration methods are seen. The third row zooms in on these highlighted circles. The final row of panels shows the aerial photograph template image after it has been registered using methods (d1) NCC, (d2) MI, (d3) NGF, (d4) SURF, and (d5) NGF-Curv.

The first case we consider is image registration of hyperspectral imagery onto LiDAR (Fig. 2). As both data sets were georeferenced by the data provider, only small distortions were present (up to 10 m) as a result of DEM or navigation inconsistencies [2], [35], [36], [40], [41]. From Fig. 2(b1)–(b5), in particular, the parts inside the circles marked on the figures [(c1)–(c5)] and the quantitative results in terms of mean, standard deviation, and correlation in Table I, we see that the results of NCC and NGF-Curv methods are better than the results of MI, NGF, and SURF methods at the expense of slow computational time. In this example, the NCC method performed as well as the NGF-Curv method, because both the hyperspectral and LiDAR images were approximately georeferenced before the registration was applied, finding a local minimum was enough to get reasonable outcomes [2].

We present two image-registration examples: one for a flat terrain and one for a rugged terrain (Figs. 3 and 4, respectively). Where topographical variation is large the correct alignment of the images becomes more difficult [2], [35], [36], [41]. The

NGF-Curv registration approach (NGF-Curv) worked well in the case of flat terrain (see Fig. 3), whereas parametric registration with three different distance measures (NCC, MI and NGF) and feature-based SURF poorly matched the detailed structures of a given reference image, see Fig. 3(b1)–(b5) in particular the parts marked by circles, which are highlighted and given in Fig. 3(c1)–(c5). NGF-Curv method provides reasonable outcomes, whereas parametric registration methods (NCC, MI and NGF) and SURF make serious mistakes and in particular, could not align detailed features [e.g., see Fig. 4(c1)–(c5)]. In addition, the quantitative analysis in Table I supports NGF-Curv outperforms other methods in both flat and rugged cases (Figs. 3 and 4) although computational time of NGF-Curv is much slower than other methods. Fig. 5 shows the results of aligning the aerial photographs onto the hyperspectral image for the cases of flat and rugged terrains in the form of a checkerboard: if the alignment is good then features such as roads and rivers should join across the checkerboard. We can clearly see that NGF-Curv method gives very accurate registration results.
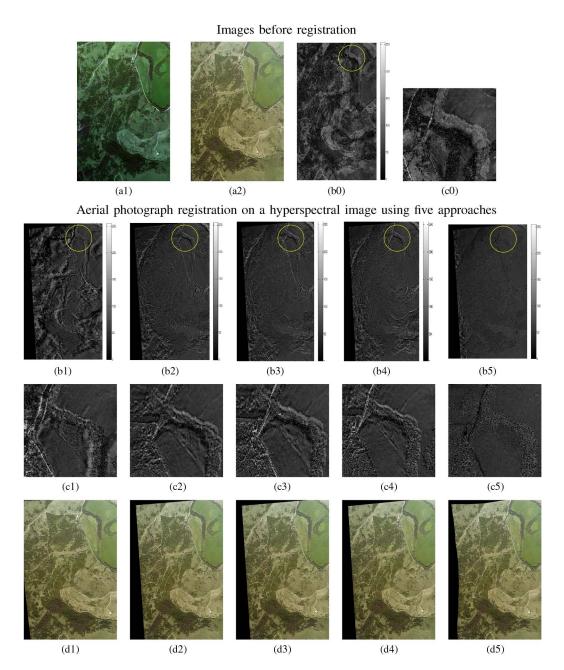
This article has been accepted for inclusion in a future issue of this journal. Content is final as presented, with the exception of pagination.

LEE *et al.*: NP IMAGE REGISTRATION OF LiDAR, HYPERSPECTRAL AND IMAGERY OF WOODED LANDSCAPES 7

Images before registration

Aerial photograph registration on a hyperspectral image using five approaches

Fig. 3. Image registration of an aerial photograph onto a hyperspectral image in a region that has flat terrain (scale 2400×1800 m^2). The first row shows (a1) a hyperspectral reference image R; (a2) an aerial photograph template image T; (b0) a map showing difference between these images (i.e., $|T - R|$); (c0) highlight the circle region of (b0). The second row shows maps of $|T_{\text{reg}} - R|$ generated by methods NCC, MI, NGF, SURF, and our NGF-Curv approach. The third row highlights the circle areas of the maps in the second row. The last row of panels shows the aerial photograph template image after it has been registered using methods (d1) NCC, (d2) MI, (d3) NGF, (d4) SURF, and (d5) NGF-Curv.

As aerial photographs were registered individually onto hyperspectral imagery there may be mismatches at the edge of each aerial photograph (visible in Figs. 3 and 4), which may produce noticeable discontinuity between the photographs. For example, in Fig. 6(c), the part marked by the red circle shows discontinuity at the interface of two aerial photographs. These boundary artifacts are due to a nonoptimal choice of the regularization parameter for the registration of aerial photographs to hyperspectral images. We chose to have a fixed regularization parameter α in (NGF-Curv), which might not be optimal for every aerial photograph in the data set, and this caused errors at the boundaries. Tuning the parameters for each

aerial photograph where discontinuity deteriorates the quality of registration can improve the result significantly. In the case of the mismatch inside the circle in Fig. 6(c) (see (e3) for the highlight of its circle region), a tuning of the regularization parameter α from 1.5×10^5 to 2×10^5 significantly improved the registration and removed the discontinuity between the two aerial photographs [Fig. 6(d) and (e4)].

VI. CONCLUSION AND OUTLOOK

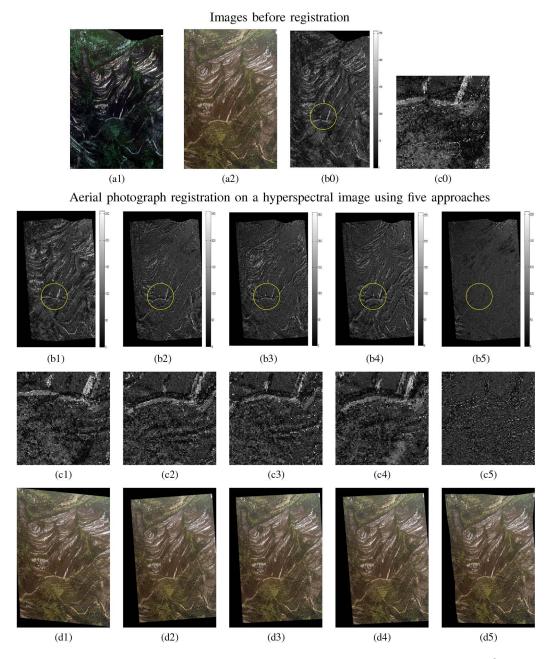The experiments illustrated in Figs. 3–5 indicate that NGF-Curv image registration techniques can effectively coalign

Images before registration

(a1) (a2) (b0) (c0)

Aerial photograph registration on a hyperspectral image using five approaches

(b1) (b2) (b3) (b4) (b5)

(c1) (c2) (c3) (c4) (c5)

(d1) (d2) (d3) (d4) (d5)

Fig. 4. Image registration of an aerial photograph onto a hyperspectral image in the case of rugged terrain (scale 2400×1800 m^2). The first row shows (a1) a hyperspectral reference image R; (a2) an aerial photograph template image T; the second row shows (b0) a map of difference between these images (i.e., $|T - R|$) for methods NCC, MI, NGF, SURF, and NGF-Curv. The third row (c0) zooms in on the circular regions of (b0). The last row of panels shows the aerial photograph template image after it has been registered using methods (d1) NCC, (d2) MI, (d3) NGF, (d4) SURF, and (d5) NGF-Curv.

remote sensing images, working as well as established methods when registration is straight forward and outperforming those approaches when dealing with nongeoreferenced photographs. Remote sensing images are usually preprocessed before being sent to users, but the orthorectification and georeferencing procedures are not accurate enough to identify individual trees. Therefore, high-accuracy registration methods for remote sensing data sets of wooded landscapes are needed.

Techniques based on feature extractions are well established in the field and are capable of accurate data assimilation in many applications. However, these approaches are difficult to apply to multisensor data, because different types of sensors may show different features, and sensor distortions are com-

plex. Intensity-based parametric methods (such as NCC, MI, and NGF) can perform fully automatic registration but assume that data are preprocessed and displacement between template and reference images is small. Feature-based parametric methods, for example, SURF, are automatic if the main features are selected both in reference and template images. However, since they depend on the features and the parametric transformation, their performance is reduced if there are many local distortions in the data.

NGF-Curv image registration provides a flexible approach allowing image registration with little prior knowledge of degree of distortion within the reference and template images. Validation of NGF-Curv with a variational formulation was
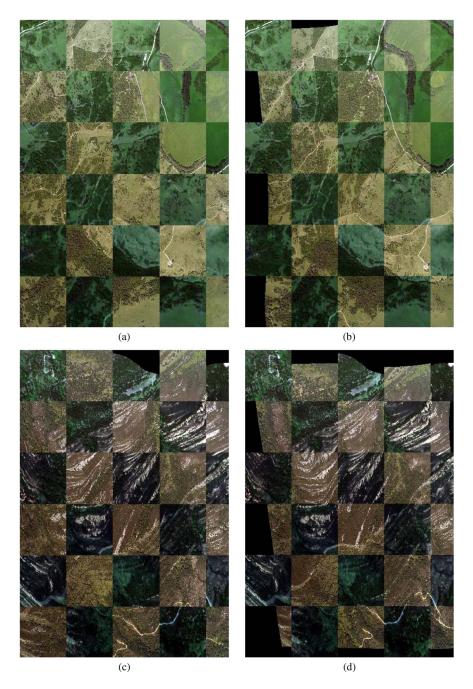
This article has been accepted for inclusion in a future issue of this journal. Content is final as presented, with the exception of pagination.

LEE *et al.*: NP IMAGE REGISTRATION OF LiDAR, HYPERSPECTRAL AND IMAGERY OF WOODED LANDSCAPES 9

Fig. 5. Checkerboard overlay between aerial photograph template images T and hyperspectral reference images R and checkerboard overlay of registered aerial photograph template images $(T_{\text{reg}}^{\text{NGF-Curv}})$ and hyperspectral reference images (R) generated by our NGF-Curv approach. (a) and (b) Flat terrain case. (c) and (d) Rugged terrain case.

demonstrated by numerical experiment in Section V. This approach can be applied to nonorthorectified images with rough geographic boundary approximation. Although most images can be registered with a fixed regularization parameter, it may lead to misalignment at the edge of the image (see Fig. 6). Further research is required to find the regularization parameter automatically, thus minimizing misalignment at the boundary.

The NGF-Curv method is designed to measure similarity between images taken by multisensors, and because it compares gradients of two images, it can handle different types of imagery. Other similarity measures, such as sum of squared distance and NCC perform poorly when applied to different

types of images. The MI method (derived from information theory) is widely used as a similarity measure in remote sensing applications as it can be applied to multisensor imaging. It measures the joint probability of image intensities and can be viewed as a generalized similarity measure [43]. However, the MI method is highly nonconvex; thus, it is difficult to optimize and increases the nonlinearity of registration [31]. Since MI is based on joint density of intensity values, it may also suffer from interpolation induced artifacts [28].

Regularization is key to the success of the NGF-Curv. Although a number of studies have used intensity-based similarity measures [14], [27]–[30], the ill-posedness of these measures

This article has been accepted for inclusion in a future issue of this journal. Content is final as presented, with the exception of pagination.

10   IEEE TRANSACTIONS ON GEOSCIENCE AND REMOTE SENSING
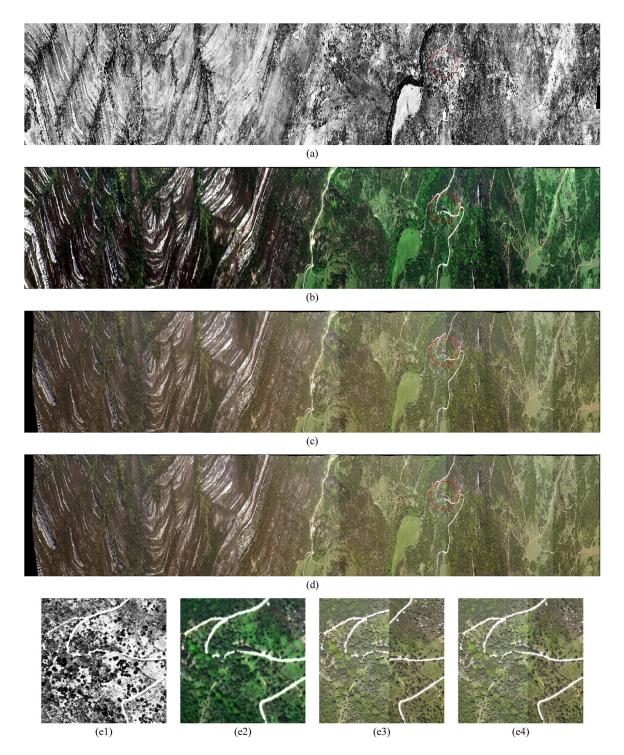

Fig. 6. Fully registered LiDAR, hyperspectral, and aerial photograph imagery. (a) LiDAR intensity image. (b) RGB bands of hyperspectral imagery. (c) Mosaic imagery of registered aerial photographs of our NGF-Curv approach with fixed global regularization parameter α. (d) Mosaic imagery of registered aerial photographs of the NGF-Curv approach with locally tuned regularization parameter α. (e1)–(e4) highlights of the circle regions in (a)–(d).

prevents their use in flexible applications in remote sensing. This means that successful image registration is conditional upon the data being preprocessed and displacement between images being small. In theory, adding a regularization term makes the problem close to, or exactly, well-posed such that the registration problem has a meaningful solution; in reality though, it is difficult to remove all local minima using this approach; thus, exact solutions are rarely achieved in reality.

A few regularization methods have been suggested to guarantee well-posedness during the registration process [46]. As aforementioned, most of these regularization techniques are sensitive to affine linear displacement such that preregistration with affine linear transformation is required [50], [55], [56]. In contrast, curvature regularization used here does not require affine preregistration steps. However, affine parametric registration at coarsest level is recommended in general applications, as

NGF-Curv still penalizes affine transformation by its boundary conditions (i.e., it is still influenced by initial position of two images to some extent, see [43], [61]).

Some aspects of NGF-Curv require further refinement. As is often the case with image registration, the NGF-Curv method is dependent on the quality of the reference image. We used LiDAR intensity images in order to register hyperspectral image. We believe the quality of LiDAR can be further improved by increasing the understanding of the radiometric properties of LiDAR intensity: LiDAR pulses do not only backscatter off the upper canopy leaves but also internal structures through penetration, and if we could filter for the information from the upper canopy, then the intensities of the LiDAR would be more similar to those from the camera or hyperspectral sensor. However, currently the AGC of Leica systems adjusts the pulse energy during the LiDAR acquisition (i.e., the pulse energy is increased when the returned energy is low). An AGC value within the range [0, 255] is given for each pulse in the LAS file, and a few studies have attempted to normalize LiDAR intensity using these numbers [52]–[54]. While none of those methods are able to successfully correct the LiDAR data sets we used, we believe that a successful radiometric calibration could indeed improve the registration accuracy.

Another difficulty is that hyperspectral and aerial photographs are strongly influenced by shading effects, because they record backscattered solar energy. If imagery is collected early or late in the day, then shaded pixels create strong gradients on one side of trees; thus, the registration process is intrinsically biased to some extent. Combining image registration with shade removal [62] could improve the quality of image registration.

Although further research on finding regularization parameter automatically is required, this research have introduced a fresh insight on image registration of remote sensing.

ACKNOWLEDGMENT

REFERENCES

[1] Y. Bentoutou, N. Taleb, K. Kpalma, and J. Ronsin, "An automatic image registration for applications in remote sensing," *IEEE Trans. Geosci. Remote Sens.*, vol. 43, no. 9, pp. 2127–2137, Sep. 2005.

[2] D. Brunner, G. Lemoine, and L. Bruzzone, "Earthquake damage assessment of buildings using VHR optical and SAR imagery," *IEEE Trans. Geosci. Remote Sens.*, vol. 48, no. 5, pp. 2403–2420, May 2010.

[3] G. Asner *et al.*, "Carnegie airborne observatory: In-flight fusion of hyperspectral imaging and waveform light detection and ranging for 3-D studies of ecosystems," *J. Appl. Remote Sens.*, vol. 1, no. 1, Sep. 2007, Art. ID. 031536.

[4] M. Dalponte, L. Bruzzone, and D. Gianelle, "Fusion of hyperspectral and LiDAR remote sensing data for classification of complex forest areas," *IEEE Trans. Geosci. Remote Sens.*, vol. 46, no. 5, pp. 1416–1427, May 2008.

[5] S. Huang, R. Crabtree, C. Potter, and P. Gross, "Estimating the quantity and quality of coarse woody debris in yellowstone post-fire forest ecosystem from fusion of SAR and optical data," *Remote Sens. Environ.*, vol. 113, no. 9, pp. 1926–1938, Sep. 2009.

[6] M. Lefsky, W. Cohen, G. Parker, and D. Harding, "Lidar remote sensing for ecosystem studies Lidar, an emerging remote sensing technology that directly measures the 3-D distribution of plant canopies, can accurately estimate vegetation structural attributes and should be of particular interest to forest, landscape, and global ecologists," *BioScience*, vol. 52, no. 1, pp. 19–30, Jan. 2002.

[7] K. Lim, P. Treitz, M. Wulder, B. St-Onge, and M. Flood, "Lidar remote sensing of forest structure," *Progress Phys. Geography*, vol. 27, no. 1, pp. 88–106, 2003.

[8] G. Asner *et al.*, "Invasive plants transform the 3-D structure of rain forests," *Proc. Nat. Acad. Sci.*, vol. 105, no. 11, pp. 4519–4523, Mar. 2008.

[9] A. Hudak and C. Wessman, "Textural analysis of historical aerial photography to characterize woody plant encroachment in South African savanna," *Remote Sens. Environ.*, vol. 66, no. 3, pp. 317–330, Dec. 1998.

[10] T. Nakashizuka, T. Katsuki, and H. Tanaka, "Forest canopy structure analyzed by using aerial photographs," *Ecological Res.*, vol. 10, no. 1, pp. 13–18, Apr. 1995.

[11] G. Asner *et al.*, "Invasive species detection in Hawaiian rainforests using airborne imaging spectroscopy and LiDAR," *Remote Sens. Environ.*, vol. 112, no. 5, pp. 1942–1955, May 2008.

[12] G. Asner, "Tropical forest carbon assessment: Integrating satellite and airborne mapping approaches," *Environ. Res. Lett.*, vol. 4, no. 3, Jul.–Sep. 2009, Art. ID. 034009.

[13] G. Asner and R. Martin, "Canopy phylogenetic, chemical and spectral assembly in a lowland Amazonian forest," *New Phytologist*, vol. 189, no. 4, pp. 999–1012, Mar. 2011.

[14] B. Zitova and J. Flusser, "Image registration methods: A survey," *Image Vis. Comput.*, vol. 21, no. 11, pp. 977–1000, Oct. 2003.

[15] J. L. Moigne, N. Netanyahu, and R. Eastman, *Image Registration for Remote Sensing*. Cambridge, U.K.: Cambridge Univ. Press, 2011.

[16] L. Brown, "A survey of image registration techniques," *ACM Comput. Surveys*, vol. 24, no. 4, pp. 325–376, Dec. 1992.

[17] H. Li, B. Manjunath, and S. Mitra, "A contour-based approach to multisensor image registration," *IEEE Trans. Image Process.*, vol. 4, no. 3, pp. 320–334, Mar. 1995.

[18] Y. Yang and X. Gao, "Remote sensing image registration via active contour model," *AEU-Int. J. Electron. Commun.*, vol. 63, no. 4, pp. 227–234, Apr. 2009.

[19] D. Lowe, "Distinctive image features from scale-invariant keypoints," *Int. J. Comput. Vis.*, vol. 60, no. 2, pp. 91–110, Nov. 2004.

[20] Q. Li, G. Wang, J. Liu, and S. Chen, "Robust scale-invariant feature matching for remote sensing image registration," *IEEE Geosci. Remote Sens. Lett.*, vol. 6, no. 2, pp. 287–291, Apr. 2009.

[21] H. Goncalves, L. Corte-Real, and J. Goncalves, "Automatic image registration through image segmentation and SIFT," *IEEE Geosci. Remote Sens. Trans.*, vol. 49, no. 7, pp. 2589–2600, Jul. 2011.

[22] M. Wahed, G. El-tawel, and A. El-karim, "Automatic image registration technique of remote sensing images," *Int. J. Adv. Comput. Sci. Appl.*, vol. 4, no. 2, Nov. 2013.

[23] M. Fischler and R. Bolles, "Random sample consensus: A paradigm for model fitting with applications to image analysis and automated cartography," *Commun. ACM*, vol. 24, no. 6, pp. 381–395, Jun. 1981.

[24] T. Kim and Y. Im, "Automatic satellite image registration by combination of matching and random sample consensus," *IEEE Trans. Geosci. Remote Sens.*, vol. 41, no. 5, pp. 1111–1117, May 2003.

[25] H. Goncalves, J. Goncalves, and L. Corte-Real, "Hairis: A method for automatic image registration through histogram-based image segmentation," *IEEE Trans. Image Process.*, vol. 20, no. 3, pp. 776–789, Mar. 2011.

[26] A. Wong and D. Clausi, "ARRSI: Automatic registration of remote-sensing images," *IEEE Trans. Geosci. Remote Sens.*, vol. 45, no. 5, pp. 1483–1493, May 2007.

[27] H. Chen, M. Arora, and P. Varshney, "Mutual information-based image registration for remote sensing data," *Int. J. Remote Sens.*, vol. 24, no. 18, pp. 3701–3706, 2003.

[28] H. Chen, P. Varshney, and M. Arora, "Performance of mutual information similarity measure for registration of multitemporal remote sensing images," *IEEE Trans. Geosci. Remote Sens.*, vol. 41, no. 11, pp. 2445–2454, Nov. 2003.

[29] S. Suri and P. Reinartz, "Mutual-information-based registration of TerraSAR-X and Ikonos imagery in urban areas," *IEEE Trans. Geosci. Remote Sens.*, vol. 48, no. 2, pp. 939–949, Feb. 2010.

[30] E. Parmehr, C. Fraser, C. Zhang, and J. Leach, "Automatic registration of optical imagery with 3D LiDAR data using statistical similarity," *ISPRS J. Photogramm. Remote Sens.*, vol. 88, pp. 28–40, Feb. 2014.

[31] E. Haber and J. Modersitzki, "Intensity gradient based registration and fusion of multi-modal images," in *Proc. MICCAI*, 2006, pp. 726–733.

This article has been accepted for inclusion in a future issue of this journal. Content is final as presented, with the exception of pagination.

12   IEEE TRANSACTIONS ON GEOSCIENCE AND REMOTE SENSING

[32] D. Kroon and C. Slump, "MRI modalitiy transformation in demon registration," in *Proc. IEEE ISBI: Nano Macro*, 2009, pp. 963–966.

[33] L. Fonseca and B. Manjunath, "Registration techniques for multisensor remotely sensed imagery," *PE RS-Photogramm. Eng. Remote Sens.*, vol. 62, no. 9, pp. 1049–1056, 1996.

[34] G. Hong and Y. Zhang, "Wavelet-based image registration technique for high-resolution remote sensing images," *Comput. Geosci.*, vol. 34, no. 12, pp. 1708–1720, Dec. 2008.

[35] J. Liang *et al.*, "Automatic registration of multisensor images using an integrated spatial and mutual information (SMI) metric," *IEEE Trans. Geosci. Remote Sens.*, vol. 51, no. 1, pp. 603–615, Jan. 2014.

[36] Y. Ye and J. Shan, "A local descriptor based registration method for multispectral remote sensing images with non-linear intensity differences," *ISPRS J. Photogramm. Remote Sens.*, vol. 90, pp. 83–95, Apr. 2014.

[37] H. Bay, A. Ess, T. Tuytelaars, and L. Gool, "Speeded-up robust features (surf)," *Comput. Vis. Image Understand.*, vol. 110, no. 3, pp. 346–359, Jun. 2008.

[38] A. Cole-Rhodes, K. Johnson, J. L. Moigne, and I. Zavorin, "Multiresolution registration of remote sensing imagery by optimization of mutual information using a stochastic gradient," *IEEE Trans. Image Process.*, vol. 12, no. 12, pp. 1495–1511, Dec. 2003.

[39] J. Hadamard, "Sur les problèmes aux dérivées partielles et leur signification physique," *Princeton Univ. Bull.*, vol. 13, no. 49–52, p. 28, 1902.

[40] J. Inglada and A. Giros, "On the possibility of automatic multisensor image registration," *IEEE Trans. Geosci. Remote Sens.*, vol. 42, no. 10, pp. 2104–2120, Oct. 2004.

[41] P. Bunting, R. Lucas, and F. Labrosse, "An area based technique for image-to-image registration of multi-modal remote sensing data," in *Proc. IEEE IGARSS*, 2008, vol. 5, pp. V-212–V-215.

[42] M. Bueger, *Geometry I*.   Berlin, Germany: Springer-Verlag, 1987.

[43] J. Modersitzki, *FAIR: Flexible Algorithms for Image Registration*. Philadelphia, PA, USA: SIAM, 2009, vol. 6.

[44] A. Sotiras, C. Davatzikos, and N. Paragios, "Deformable medical image registration: A survey," *IEEE Trans. Med. Imaging*, vol. 32, no. 7, pp. 1153–1190, Jul. 2013.

[45] A. D. Leow *et al.*, "Statistical properties of Jacobian maps and the realization of unbiased large-deformation nonlinear image registration," *IEEE Trans. Med. Imaging*, vol. 26, no. 6, pp. 822–832, Jun. 2007.

[46] M. Burger, J. Modersitzki, and L. Ruthotto, "A hyperelastic regularization energy for image registration," *SIAM J. Sci. Comput.*, vol. 35, no. 1, pp. B132–B148, 2013.

[47] M. Chiang *et al.*, "Fluid registration of diffusion tensor images using information theory," *IEEE Trans. Med. Imaging*, vol. 27, no. 4, pp. 442–456, Apr. 2008.

[48] M. Beg, M. Miller, A. Trouvé, and L. Younes, "Computing large deformation metric mappings via geodesic flows of diffeomorphisms," *Int. J. Comput. Vis.*, vol. 61, no. 2, pp. 139–157, Feb. 2005.

[49] T. Vercauteren, X. Pennec, A. Perchant, and N. Ayache, "Diffeomorphic demons: Efficient non-parametric image registration," *NeuroImage*, vol. 45, no. 1, pp. S61–S72, Mar. 2009.

[50] B. Fischer and J. Modersitzki, "Curvature based image registration," *J. Math. Imaging Vis.*, vol. 18, no. 1, pp. 81–85, 2003.

[51] S. Dawn, V. Saxena, and B. Sharma, "Remote sensing image registration techniques: A survey," in *Image and Signal Processing*.   Berlin, Germany: Springer-Verlag, 2010, pp. 103–112.

[52] S. Kaasalainen *et al.*, "Radiometric calibration of LiDAR intensity with commercially available reference targets," *IEEE Trans. Geosci. Remote Sens.*, vol. 47, no. 2, pp. 588–598, Feb. 2009.

[53] I. Korpela, H. Ørka, J. Hyyppä, V. Heikkinen, and T. Tokola, "Range and AGC normalization in airborne discrete-return LiDAR intensity data for forest canopies," *ISPRS J. Photogramm. Remote Sens.*, vol. 65, no. 4, pp. 369–379, Jul. 2010.

[54] I. Korpela *et al.*, "Tree species classification using airborne LiDAR— Effects of stand and tree parameters, downsizing of training set, intensity normalization, and sensor type," *Silva Fennica*, vol. 44, no. 2, pp. 319–339, 2010.

[55] B. Fischer and J. Modersitzki, "A unified approach to fast image registration and a new curvature based registration technique," *Linear Algebra Appl.*, vol. 380, pp. 107–124, 2004.

[56] J. Modersitzki, *Numerical Methods for Image Registration*.   Oxford, U.K.: Oxford Univ. Press, 2003.

[57] G. Christensen, "Deformable shape models for anatomy," Ph.D. dissertation, Washington Univ. Saint Louis, St. Louis, MO, USA, 1994.

[58] M. Bro-Nielsen and C. Gramkow, "Fast fluid registration of medical images," *Vis. Biomed. Comput.*, vol. 1131, pp. 265–276, 1996.

[59] E. Haber and J. Modersitzki, "A multilevel method for image registration," *SIAM J. Sci. Comput.*, vol. 27, no. 5, pp. 1594–1607, 2006.

[60] U. Ascher, E. Haber, and H. Huang, "On effective methods for implicit piecewise smooth surface recovery," *SIAM J. Sci. Comput.*, vol. 28, no. 1, pp. 339–358, 2006.

[61] S. Henn, "A full curvature based algorithm for image registration," *J. Math. Imaging Vis.*, vol. 24, no. 2, pp. 195–208, Mar. 2006.

[62] G. Finlayson, M. Drew, and C. Lu, "Entropy minimization for shadow removal," *Int. J. Comput. Vis.*, vol. 85, no. 1, pp. 35–57, Oct. 2009.

Juheon Lee is currently working toward the Ph.D. degree in the Department of Plant Sciences, University of Cambridge, Cambridge, U.K.

Since 2012, he has been with the Department of Plant Sciences, and Applied Mathematics and Theoretical Physics, University of Cambridge. His research interests include image registration and segmentation in remote sensing.

Xiaohao Cai received the M.S. degree in mathematics from Zhejiang University, Hangzhou, China, in 2008, and the Ph.D. degree in mathematics from The Chinese University of Hong Kong, Hong Kong, in 2012.

He is currently a Postdoctoral Researcher with the Department of Plant Sciences, and the Department of Applied Mathematics and Theoretical Physics, University of Cambridge, Cambridge, U.K. His research interests include image processing, numerical analysis, and their applications in processing of digital image, video, biomedical imaging, remote sensing data, just to name a few.

Carola-Bibiane Schönlieb received the diploma degree from the Institute for Mathematics, University of Salzburg, Salzburg, Austria, in 2004 and the Ph.D. degree from the University of Cambridge, Cambridge, U.K., in 2009.

From 2004 to 2005, she held a teaching position in Salzburg. After one year of postdoctoral activity at the University of Göttingen, Göttingen, Germany, since 2010, she has been a Lecturer in applied and computational analysis with the Department of Applied Mathematics and Theoretical Physics, University of Cambridge (U.K.). There, she is Head of the Cambridge Image Analysis group and, since 2011, a Fellow of Jesus College Cambridge. Her current research interests range from nonlinear partial differential equations to computational and convex analysis, with applications in digital image processing and inverse problems in imaging.

David A. Coomes joined the staff of the Plant Sciences Department of Cambridge University in 2000. He is head of the Forest Ecology and Conservation Group. His current interests research include modeling the impacts of anthropogenic global change using large-scale forest inventories, and developing approaches for mapping forest change using airborne remote sensing technologies.